

# A large-gap magnetic topological heterostructure formed by subsurface incorporation of a ferromagnetic layer

Toru Hirahara,<sup>\*,†</sup> Sergey V. Eremeev,<sup>‡,¶,§,||</sup> Tetsuroh Shirasawa,<sup>⊥,§§</sup> Yuma Okuyama,<sup>†</sup> Takayuki Kubo,<sup>#</sup> Ryosuke Nakanishi,<sup>#</sup> Ryota Akiyama,<sup>#</sup> Akari Takayama,<sup>#</sup> Tetsuya Hajiri,<sup>@,|||</sup> Shin-ichiro Ideta,<sup>@</sup> Masaharu Matsunami,<sup>@,⊥⊥</sup> Kazuki Sumida,<sup>△</sup> Koji Miyamoto,<sup>▽</sup> Yasumasa Takagi,<sup>††</sup> Kiyohisa Tanaka,<sup>@</sup> Taichi Okuda,<sup>▽</sup> Toshihiko Yokoyama,<sup>††</sup> Shin-ichi Kimura,<sup>@,##</sup> Shuji Hasegawa,<sup>#</sup> and Evgueni V. Chulkov<sup>||,‡‡,¶¶,¶,§</sup>

<sup>†</sup>*Department of Physics, Tokyo Institute of Technology, Tokyo 152-8551, Japan*

<sup>‡</sup>*Institute of Strength Physics and Materials Science, Tomsk, 634055, Russia*

<sup>¶</sup>*Tomsk State University, Tomsk, 634050, Russia*

<sup>§</sup>*Saint Petersburg State University, Saint Petersburg, 198504, Russia*

<sup>||</sup>*Donostia International Physics Center (DIPC), Paseo de Manuel Lardizabal, 4, 20018 San Sebastián/Donostia, Basque Country, Spain*

<sup>⊥</sup>*Institute for Solid State Physics, University of Tokyo, Kashiwa 277-8581, Japan*

<sup>#</sup>*Department of Physics, University of Tokyo, Tokyo 113-0033, Japan*

<sup>@</sup>*UVSOR Facility, Institute for Molecular Science, Okazaki 444-8585, Japan*

<sup>△</sup>*Graduate School of Science, Hiroshima University, Higashi-Hiroshima 739-8526, Japan*

<sup>▽</sup>*Hiroshima Synchrotron Radiation Center, Hiroshima University, Higashi-Hiroshima 739-8526, Japan*

<sup>††</sup>*Department of Materials Molecular Science, Institute for Molecular Science, Okazaki 444-8585, Japan*

<sup>‡‡</sup>*Departamento de Física de Materiales, Facultad de Ciencias Químicas, UPV/EHU, Apdo. 1072, 20080 San Sebastián, Basque Country, Spain*

<sup>¶¶</sup>*Centro de Física de Materiales, CFM-MPC, Centro Mixto CSIC-UPV/EHU, Apdo.1072, 20080 San Sebastián/Donostia, Basque Country, Spain*

<sup>§§</sup>*Present address: National Institute of Advanced Industrial Science and Technology, Ibaraki 305-8560, Japan*

<sup>|||</sup>*Present address: Department of Crystalline Materials Science, Nagoya University, Nagoya 464-8603, Japan*

<sup>⊥⊥</sup>*Present address: Energy Materials Laboratory, Toyota Technological Institute, Nagoya 468-8511, Japan*

<sup>##</sup>*Present address: Graduate School of Frontier Biosciences and Department of Physics, Osaka University, Suita 565-0871, Japan*

E-mail: hirahara@phys.titech.ac.jp

Phone: +81 (0)3 5734 2365. Fax: +81 (0)3 5734 2365

## Abstract

Inducing magnetism into topological insulators is intriguing for utilizing exotic phenomena such as the quantum anomalous Hall effect (QAHE) for technological applications. While most studies have focused on doping magnetic impurities to open a gap at the surface-state Dirac point, many undesirable effects have been reported to appear in some cases that makes it difficult to determine whether the gap opening is due to the time-reversal symmetry breaking or not. Furthermore, the realization of the QAHE has been limited to low temperatures. Here we have succeeded in generating a massive Dirac cone in a  $\text{MnBi}_2\text{Se}_4/\text{Bi}_2\text{Se}_3$  heterostructure which was fabricated by self-assembling a  $\text{MnBi}_2\text{Se}_4$  layer on top of the  $\text{Bi}_2\text{Se}_3$  surface as a result of the co-deposition of Mn and Se. Our experimental results, supported by relativistic *ab initio* calculations, demonstrate that the fabricated  $\text{MnBi}_2\text{Se}_4/\text{Bi}_2\text{Se}_3$  heterostructure shows ferromagnetism up to room temperature and a clear Dirac-cone gap opening of  $\sim 100$  meV without any other significant changes in the rest of the band structure. It can be considered as a result of the direct interaction of the surface Dirac cone and the magnetic layer rather than a magnetic proximity effect. This spontaneously formed self-assembled heterostructure with a massive Dirac spectrum, characterized by a nontrivial Chern number  $C = -1$ , has a potential to realize the QAHE at significantly higher temperatures than reported up to now and can serve as a platform for developing future “topotronics” devices.

## Keywords

Topological insulators, Magnetism, Massive Dirac cone, Quantum anomalous Hall effect

Classification of materials and phases based on the “topological properties” of the system has become one of the most extensively studied research fields in physics and was the topic for the Nobel prize in physics in 2016.<sup>1</sup> Topological insulators (TIs) are insulating materials

1  
2  
3  
4  
5  
6 that have metallic surface states, whose electron spins are locked to their momentum.<sup>2,3</sup>  
7  
8 In the simplest case, the surface states are helical Dirac fermions and the Dirac point is  
9  
10 robust due to the protection by time-reversal symmetry. When the time-reversal symmetry  
11  
12 is broken in TIs, novel quantum phenomena have been predicted to occur including the  
13  
14 formation of magnetic monopoles,<sup>4</sup> the quantum anomalous Hall effect (QAHE),<sup>5</sup> and the  
15  
16 topological magnetoelectric effect.<sup>6</sup>  
17

18  
19 In terms of the electronic structure, a magnetic TI is expected to host a massive Dirac  
20  
21 cone with a band gap. Many researches have been performed to induce magnetism in TIs by  
22  
23 magnetic impurity doping when growing thin films.<sup>7,8</sup> Although it seemed that this was the  
24  
25 most efficient way with the successful observation of the QAHE in Cr or V-doped  $(\text{Bi,Sb})_2\text{Te}_3$   
26  
27 thin films,<sup>8-10</sup> the precise quantization of the Hall resistance at zero field is still only limited  
28  
29 to low temperature (10-100 mK). The temperature for the realization of the QAHE ( $T_{QAHE}$ )  
30  
31 depends on the Curie temperature as well as the size of the Dirac cone gap of the system. Up  
32  
33 to now, the main obstacle in enhancing  $T_{QAHE}$  is an inhomogeneous distribution of magnetic  
34  
35 atoms over the TI film that results in strong fluctuations of the magnetic energy gap.<sup>11,12</sup>  
36  
37 Modulation doping was shown to increase  $T_{QAHE}$  and the QAHE was observed at 2 K for  
38  
39 Cr-doped  $(\text{Bi, Sb})_2\text{Te}_3$  thin films when the magnetic-doped layer was placed 1 nm below the  
40  
41 surface.<sup>13</sup> A recent theoretical work suggests that this can be enhanced by V and I co-doping  
42  
43 of  $\text{Sb}_2\text{Te}_3$ .<sup>14</sup>

44  
45 Another drawback of the magnetically doped systems is that there has been no direct  
46  
47 observation of the massive Dirac cone for the samples that show the QAHE using angle-resolved  
48  
49 photoemission spectroscopy (ARPES).<sup>15</sup> With local probes such as scanning tunneling spectroscopy  
50  
51 (STS), an inhomogeneous Dirac-cone gap was observed for Cr-doped  $(\text{Bi, Sb})_2\text{Te}_3$ .<sup>11</sup> On the  
52  
53 other hand, for V-doped  $\text{Sb}_2\text{Te}_3$ , it was reported that impurity states will reside within the  
54  
55 Dirac-cone gap and as a result, the density of states will look gapless.<sup>16</sup> Moreover, impurity  
56  
57 bands will emerge near the Dirac point and it was reported that a massive Dirac cone can  
58  
59 arise even due to a nonmagnetic origin for impurity-doped  $\text{Bi}_2\text{Se}_3$  films with ARPES<sup>17</sup> .  
60

1  
2  
3  
4  
5  
6 Thus one can say that magnetic impurity doped TI films are not promising in terms of (i)  
7 enhancing  $T_{QAHE}$  to the region where application becomes possible and (ii) clearly observing  
8 the gapped Dirac cone as a result of the time-reversal symmetry breaking in a macroscopic  
9 scale.  
10  
11  
12

13  
14 An alternative way to induce magnetism in TIs is to make a heterostructure of TIs  
15 and magnets. Such systems are also used in experiments to observe the surface-state spin  
16 transport.<sup>18–21</sup> But there has not been a direct observation of the QAHE as well as the  
17 existence of a gapped Dirac cone at the interfaces in these heterostructures. One reason for  
18 this is the absence an atomically sharp interface that makes the gap small and difficult to  
19 observe, which should be also responsible for the low spin-charge conversion efficiency. Even  
20 in some cases with a sharp interface (EuS/Bi<sub>2</sub>Se<sub>3</sub>), the Dirac-cone gap was shown not to be  
21 related with the magnetic proximity effect,<sup>22</sup> although magnetization measurements showed  
22 evidence of a magnetic interaction.<sup>23</sup> In another case of MnSe/Bi<sub>2</sub>Se<sub>3</sub>, it was shown from *ab*  
23 *initio* calculations that states other than the gapped Dirac cone will cross  $E_F$ <sup>24</sup> and make the  
24 QAHE impossible to realize. However, the measured band structure was completely different  
25 from the calculation but no clear explanation was given.<sup>25</sup> Thus the interplay between the  
26 topological properties and magnetism in an ordered layered system needs to be examined  
27 further.  
28  
29  
30  
31  
32  
33  
34  
35  
36  
37  
38  
39  
40  
41

42 In the present study, we take advantage of self-organization to produce an ideal system  
43 of a magnetic insulator/TI heterostructure, which is formed spontaneously as a hexagonal  
44 MnBi<sub>2</sub>Se<sub>4</sub> septuple layer (SL) on the basis of the topmost quintuple layer (QL) of Bi<sub>2</sub>Se<sub>3</sub>  
45 film under Mn and Se co-deposition. Due to the ferromagnetism of MnBi<sub>2</sub>Se<sub>4</sub> up to room  
46 temperature as revealed by superconducting quantum interference device (SQUID) and X-ray  
47 magnetic circular dichroism (XMCD) measurements, the Dirac cone becomes massive with a  
48 gap size of  $\sim 100$  meV. First-principles calculations show that the calculated Chern number is  
49  $C = -1$  and the heterostructure is identified as a quantum anomalous Hall phase. Our results  
50 not only show the first example of a clear Dirac-cone gap opening at the ferromagnet/TI  
51  
52  
53  
54  
55  
56  
57  
58  
59  
60

interface, but imply that this should be a suitable system to realize the QAHE at higher temperatures than previously reported by tuning the Fermi level as well as to develop novel devices based on the topological magnetoelectric effect.

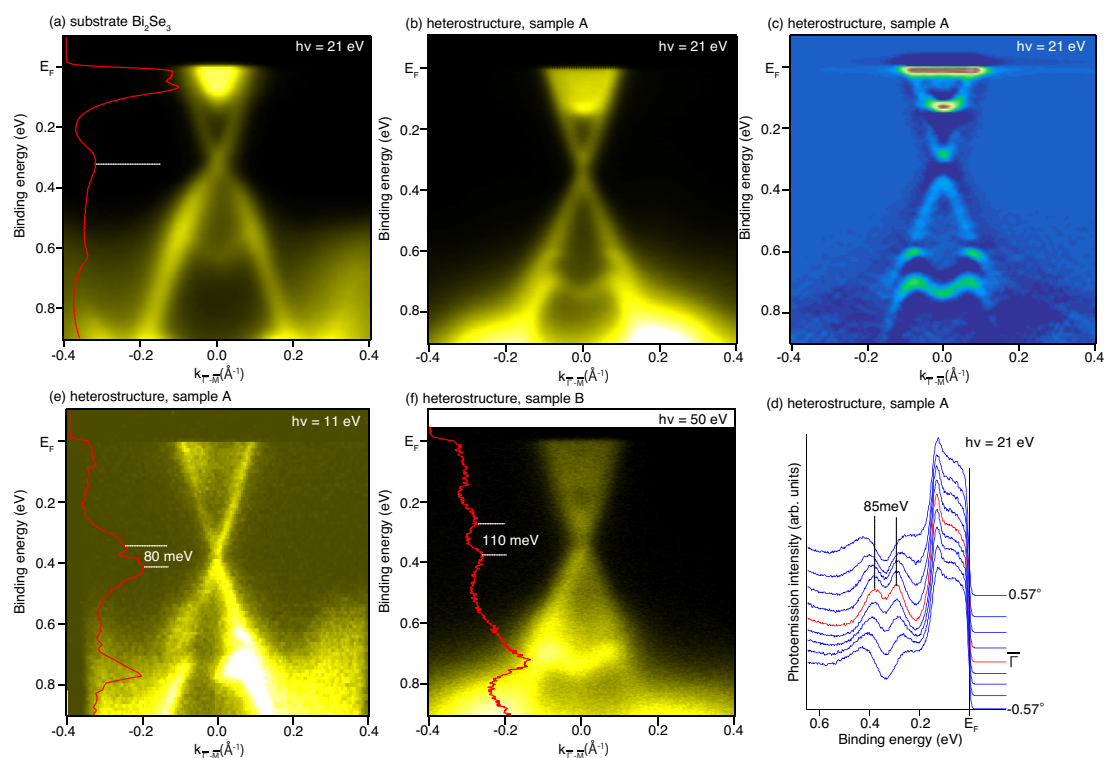


Figure 1: (a) Band dispersion of the substrate  $\text{Bi}_2\text{Se}_3$  film measured along the  $\bar{\Gamma} - \bar{M}$  direction taken at  $h\nu = 21$  eV. The red line shows the energy distribution curve (EDC) at the  $\bar{\Gamma}$  point. (b) Band dispersion of the heterostructure for sample A measured along the  $\bar{\Gamma} - \bar{M}$  direction taken at  $h\nu = 21$  eV. (c) The second derivative with respect to the energy of the band dispersion in (b). (d) Raw spectra (EDCs) near the  $\bar{\Gamma}$  point of the band dispersion in (b). The gap size of the Dirac cone is 85 meV. (e) Band dispersion of the heterostructure for sample A measured along the  $\bar{\Gamma} - \bar{M}$  direction taken at  $h\nu = 11$  eV. The gap size of the Dirac cone is 80 meV. The red line shows the EDC at the  $\bar{\Gamma}$  point. (f) Band dispersion of the heterostructure for sample B measured along the  $\bar{\Gamma} - \bar{M}$  direction taken at  $h\nu = 50$  eV. The gap size of the Dirac cone is 110 meV. The red line shows the EDC at the  $\bar{\Gamma}$  point. All the measurements were performed at 30 K.

Figure 1(a) shows the band dispersion of the  $\text{Bi}_2\text{Se}_3$  thin film which was used as the substrate for the heterostructure formation. The well-known Dirac-cone of the surface states in the bulk band gap can be seen together with the bulk conduction band at the Fermi level due to the unintentional doping. The Dirac point is recognized as shown in the energy

1  
2  
3  
4  
5  
6 distribution curve (EDC) at the  $\bar{\Gamma}$  point (red line). Figure 1(b) shows the band structure  
7 of the heterostructure (sample A) after Mn and Se were co-deposited on  $\text{Bi}_2\text{Se}_3$ . It was  
8 measured immediately after cooling down the sample. A clear gap opening is observed at  
9 the Dirac point. This becomes more prominent by making the second derivative with respect  
10 to the energy of the image in Fig. 1(b), which is shown in Fig. 1(c). The gap size is deduced  
11 as  $\sim 85$  meV from the EDCs in Fig. 1(d). A slightly smaller gap is observed when the photon  
12 energy is changed to 11 eV, as shown in Fig. 1(e). The estimated gap size is  $\sim 80$  meV, which  
13 is nearly the same as that shown in Fig. 1(d). It can also be noticed that the midpoint  
14 of the energy gap has shifted down by about 70 meV from Figs. 1(b)-(d) to Fig. 1(e), due  
15 to the band bending near the surface caused by the residual gas or defect formation,<sup>26,27</sup>  
16 since Fig. 1(e) was measured 12 hours after Figs. 1(b)-(d). The band dispersion images  
17 taken with other photon energies for sample A are shown in Fig. S1. Even though the gap  
18 exists irrespective of the Fermi level position, the gap size slightly changes depending on the  
19 measurement condition. However, there is no correlation between the mid-gap position and  
20 the gap size. Figure 1(f) shows the band dispersion image of a different sample (sample B)  
21 taken at  $h\nu = 50$  eV just after cooling down the sample posterior to the preparation. The  
22 gap size is  $\sim 110$  meV, larger than that for sample A although the midpoint of the gap is  
23 nearly the same. We have also measured the gap size for other samples and the gap value  
24 is in the range of 75-120 meV when the Dirac point is located at the binding energy of  
25 0.31-0.39 eV, although there is no correlation between the two quantities. We conclude that  
26 when Mn and Se are co-deposited on  $\text{Bi}_2\text{Se}_3$  and a heterostructure is formed, the Dirac cone  
27 becomes gapped. At first glance, it should be due to the magnetic proximity effect from  
28 antiferromagnetic MnSe.  
29  
30  
31  
32  
33  
34  
35  
36  
37  
38  
39  
40  
41  
42  
43  
44  
45  
46  
47  
48  
49  
50  
51

52 However, there is one contradictory point about this band dispersion of the heterostructure.  
53 According to *ab initio* calculations,<sup>24</sup> the band dispersion of a MnSe/ $\text{Bi}_2\text{Se}_3$  heterostructure  
54 should have the following characteristics: (i) a massive Dirac cone with a gap of 8.5 meV, (ii)  
55 other metallic states in the  $\text{Bi}_2\text{Se}_3$  bulk band gap. In our experimental data, we do not find  
56  
57  
58  
59  
60

any additional states in the Dirac state energy region. Moreover, the gap size is an order of magnitude larger than that predicted in the calculation. Therefore, the calculation and the experiment are not consistent with each other. Various factors may be responsible for this inconsistency, such as the difference in the interface structure or the thickness of the MnSe layers. We have therefore performed structure analyses of the heterostructure based on the LEED *IV* technique to resolve this inconsistency.

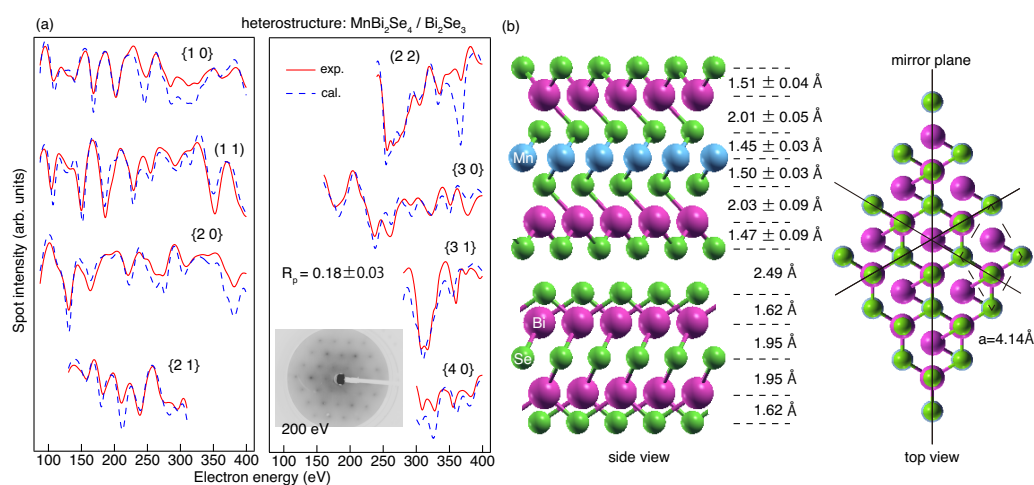


Figure 2: (a) Experimental *IV* spectra of LEED spots measured at 100 K for the heterostructure (red solid lines), and the calculated spectra of the optimized model shown in (b) (blue dotted lines). The inset shows the LEED pattern at 200 eV. (b) Cross-sectional (left) and top (right) view of the optimized model of the heterostructure, which turns out to be MnBi<sub>2</sub>Se<sub>4</sub>/Bi<sub>2</sub>Se<sub>3</sub>. Blue, pink, and green atoms represent Mn, Bi, and Se respectively. The solid lines show the mirror plane and the dotted parallelogram shows the unit cell.

Figure 2(a) shows the experimentally observed *IV* curves (red solid lines). To reproduce these curves, we have first assumed the MnSe/Bi<sub>2</sub>Se<sub>3</sub> heterostructure that is expected from the sample preparation method. However, we could not obtain R-factor ( $R_p$ ) values smaller than 0.4. Thus it was proven that the heterostructure we have fabricated was not MnSe/Bi<sub>2</sub>Se<sub>3</sub>. We tried other structures and finally found one that was in striking agreement with the experimental LEED *IV* curves. The calculated *IV* curves for the optimized structure are shown by the blue-dotted lines in Fig. 2(a). The agreement between the two curves is excellent with  $R_p = 0.18 \pm 0.03$ . The structure thus determined is shown in Fig. 2(b). What is remarkable about this structure is that the deposited Mn and Se are not on top

of the  $\text{Bi}_2\text{Se}_3$  substrate, but they are incorporated inside the topmost QL of  $\text{Bi}_2\text{Se}_3$ . So we can say that a  $\text{MnBi}_2\text{Se}_4$  septuple layer (SL) spontaneously forms on top of  $\text{Bi}_2\text{Se}_3$  by self-organization. Although the microscopic mechanism of MnSe bilayer immersion into the QL is not clear, our calculations show that the  $\text{MnBi}_2\text{Se}_4$  SL is 630 meV energetically more favorable as compared to the MnSe bilayer (BL)/ $\text{Bi}_2\text{Se}_3$ -QL interface.  $\text{MnBi}_2\text{Se}_4$  in the bulk form is reported to have the monoclinic structure with  $C2/m$  symmetry. It is shown to be a narrow gap semiconductor and antiferromagnetic with  $T_{N\text{eel}} \sim 14$  K.<sup>28</sup> However, the  $\text{MnBi}_2\text{Se}_4$  SL that we have fabricated has a hexagonal structure and is a semiconductor with a gap of  $\sim 0.4$  eV (Fig. S3).

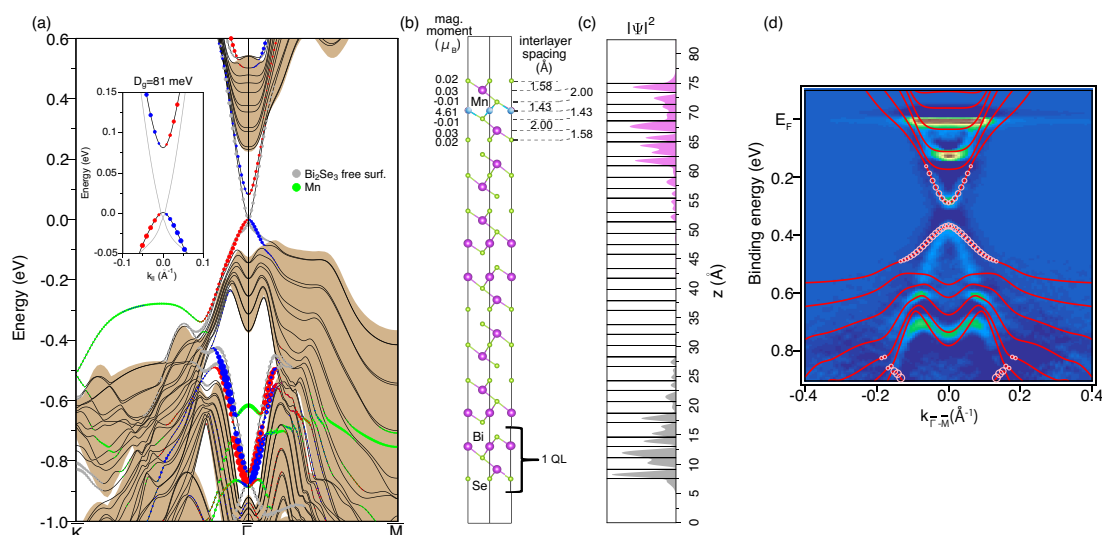


Figure 3: (a) Calculated band dispersion of a  $\text{MnBi}_2\text{Se}_4/6$  QL  $\text{Bi}_2\text{Se}_3$  heterostructure. The states marked in red and blue are localized at the topmost SL and the next  $\text{Bi}_2\text{Se}_3$  QL and spin-polarized in the in-plane direction perpendicular to the wavenumber (positive and negative, respectively). The states marked in green are the ones mostly localized at  $\text{MnBi}_2\text{Se}_4$  SL and labeled “Mn”. The states localized at the bottom surface of the slab are indicated in gray. The shaded area shows the bulk band projection of  $\text{Bi}_2\text{Se}_3$ . The inset shows a close-up of the Dirac-state dispersion. A gap of 81 meV is found for the Dirac cone at the top surface. (b) The real space atomic configuration used in the calculation together with the interlayer spacings and layer-resolved magnetic moments. (c) Wave-function ( $|\Psi|^2$ ) plot for the gapped Dirac state at the top surface (violet), and that at the bottom surface (gray), respectively. (d) The calculated band dispersion overlapped with the experimental data of Fig. 1 (c). Pink circles show the states localized in the SL.

The electronic structure of the heterostructure was calculated based on the determined



1  
2  
3  
4  
5  
6 atomic structure of Fig. 2(b). Namely, a six QL film of  $\text{Bi}_2\text{Se}_3$  was sandwiched between  
7  
8  $\text{MnBi}_2\text{Se}_4$  and vacuum. The interlayer spacing values obtained after structural relaxation of  
9  
10 the heterostructure and shown in Fig. 3(b) are in excellent agreement with the experimentally  
11  
12 determined values shown in Fig. 2(b). We found that the spin structure with the Mn  
13  
14 magnetic moment pointing out-of-plane is 0.2 meV energetically more favorable than the  
15  
16 one with in-plane spin polarization and the magnetic moment of Mn was found to be  
17  
18  $4.61 \mu_B$  (Fig. 3(b)). The calculated band dispersion is shown in Fig. 3(a). The red and  
19  
20 blue points correspond to the states with in-plane spin polarization perpendicular to the  
21  
22 wavenumber (positive and negative, respectively) that are localized at the topmost SL and  
23  
24 the neighboring QL (refer to the supplementary material for the experimental results of  
25  
26 the Dirac-cone spin-polarization). Near the Fermi level, the massless Dirac cone of pristine  
27  
28  $\text{Bi}_2\text{Se}_3$  at the bottom surface can be found (gray points and gray line in inset) together with  
29  
30 the massive Dirac state with a gap  $D_g=81$  meV at the top surface. The “gray” band can be  
31  
32 a good reference for tracking the changes in the Dirac state. As can be seen, the lower part  
33  
34 of the Dirac cone of the gapped state shows almost no change in the energy position and the  
35  
36 gap is formed by shifting up the upper branch. The calculations performed for a symmetric  
37  
38 heterostructure, where  $\text{Bi}_2\text{Se}_3$  is sandwiched between two  $\text{MnBi}_2\text{Se}_4$  SLs, result in the same  
39  
40 value of the Dirac-cone gap. Figure 3(d) shows this calculated spectrum overlapped with the  
41  
42 experimental result (the calculation was rigidly shifted by -0.38 eV to fit to the experimental  
43  
44  $E_F$ ). The agreement between the two is excellent with exception of flatter dispersion of the  
45  
46 bottom part of the Dirac cone in the calculation whereas the gap size in the Dirac cone, as  
47  
48 well as fine structures other than the Dirac cone, are well reproduced. The green points in  
49  
50 Fig. 3(a) are states localized at the topmost SL and labeled “Mn” because it has the maximum  
51  
52 contribution from the Mn  $p_z$  orbitals. They are located along the  $\bar{\Gamma} - \bar{K}$  direction in the  
53  
54  $\text{Bi}_2\text{Se}_3$  bulk band gap and a band that resembles this is also found in the calculated dispersion  
55  
56 of the free-standing  $\text{MnBi}_2\text{Se}_4$  SL (Fig. S3). This was actually observed experimentally when  
57  
58 we performed ARPES measurements along the  $\bar{\Gamma} - \bar{K}$ , as shown in Fig. S9(a). Altogether,  
59  
60

1  
2  
3  
4  
5  
6 the calculation reproduces the experimentally observed band structure nicely, and we are  
7 sure that the heterostructure we have fabricated is  $\text{MnBi}_2\text{Se}_4/\text{Bi}_2\text{Se}_3$ . Moreover, one can say  
8 that the mass acquisition of the Dirac cone is not due to a magnetic proximity effect because  
9 the Dirac state and the magnetic layer are both at the topmost SL (70% of the Dirac state  
10 is localized in the SL, see Fig. 3(c)). We should rather say that this is a “direct interaction”  
11 between the magnetic layer and the surface Dirac cone, since they overlap in real space and  
12 some part of the wave-function of the Dirac state is within the Mn layers. The original Dirac  
13 cone of  $\text{Bi}_2\text{Se}_3$  has been pushed up to the newly formed  $\text{MnBi}_2\text{Se}_4$  capping layer, similar to  
14 that in other topological-insulator based heterostructures discussed in Ref. 29. This is the  
15 reason why there is a large gap of  $\sim 80$  meV at the Dirac point, in contrast to the case of  
16  $\text{MnSe}/\text{Bi}_2\text{Se}_3$  where a magnetic proximity effect was considered.<sup>24</sup>  
17  
18  
19  
20  
21  
22  
23  
24  
25  
26  
27

28 The gapped Dirac state has a potential to realize the QAHE. The quantized Hall conductance  
29  $\sigma_{yx} = Ce^2/h$  is related to the topological characteristic of the band structure known as the  
30 Chern number  $C$ .<sup>30</sup> Our calculations show that the gapped spectrum of the  $\text{MnBi}_2\text{Se}_4/\text{Bi}_2\text{Se}_3$   
31 heterostructure is characterized by the Chern number  $C = -1$ , that defines the obtained  
32 heterostructure unambiguously as a quantum anomalous Hall phase. To confirm the topological  
33 character of the heterostructure spectrum, we artificially decreased the spin-orbit interaction  
34 strength  $\lambda$  and found that it leads to the gap narrowing and its closing at  $\lambda/\lambda_0 \approx 0.75$  (see  
35 Fig. S4). Upon further decrease of the spin-orbit interaction strength, the gap reopens and  
36 the system becomes a topologically trivial insulator.  
37  
38  
39  
40  
41  
42  
43  
44  
45

46 Next, we have tried to experimentally verify the absence of time-reversal symmetry in  
47 the heterostructure as the calculation suggests. Figures 4(a) and (b) show the magnetization  
48 curves measured with SQUID for the Se-capped sample B taken at 4 K (a) and at 300 K (b),  
49 respectively. The magnetic field was applied perpendicular to the sample surface (The data  
50 for the in-plane magnetization can be found in Fig. S7). In order to display the situation near  
51 zero-field clearly, we show in the inset the close-up for -0.1 to 0.1 T. There is a vivid hysteresis  
52 loop both at 4 K and 300 K, demonstrating the ferromagnetic nature of the heterostructure.<sup>31</sup>  
53  
54  
55  
56  
57  
58  
59  
60

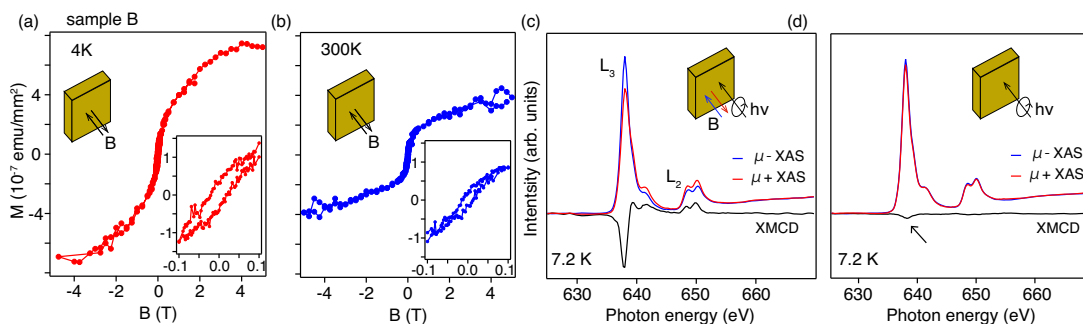


Figure 4: (a),(b) Magnetization curves measured with SQUID for the Se-capped sample B taken at 4 K (a) and at 300 K (b), respectively. The magnetic field was applied perpendicular to the sample surface. The inset shows the close-up near zero-field. Clear hysteresis loops can be observed both at 4 K and 300 K. (c) X-ray absorption spectra (XAS) at 7.2 K for a circularly polarized incident light when a  $\pm 5$  T magnetic field was applied along the surface-normal direction.  $\mu_+$  and  $\mu_-$  correspond to the spectrum obtained at +5 T and -5 T, respectively. The corresponding XMCD spectrum is also shown. The Se capping layer was removed by annealing the sample in UHV. (d) Same as (c) but measured at zero field. A remanent XMCD signal can be observed (shown by the arrow).

Actually, the gapped Dirac cone can also be observed at room temperature (Fig. S2) and thus the Curie temperature is confirmed to be above 300 K also from ARPES. We also performed XMCD measurements after removing the Se cap in UHV to make sure that the Se cap is not affecting the magnetic properties. Figure 4(c) shows the X-ray absorption (XAS) spectra at the Mn  $L$  edge measured at 7.2 K for a circularly polarized incident light when a  $\pm 5$  T magnetic field was applied along the surface-normal direction.  $\mu_+$  and  $\mu_-$  correspond to the spectrum obtained at +5 T and -5 T, respectively. The corresponding XMCD spectrum is also shown and there is a clear signal. The quantitative analysis of the XMCD measurements using the sum-rule is discussed in the supplementary material, see Fig. S5. The measurements were also performed at remanence (0 T applied magnetic field), namely the signal was obtained after switching off the  $\pm 5$  T magnetic field applied perpendicular to the surface (Fig. 4(d)). Although weak (the peak at the  $L_3$  edge is  $\sim 7\%$  compared to the data of Fig. 4(c)), we still can notice the XMCD signal (the arrow in Fig. 4(d)) and this confirms that the system is ferromagnetic. We believe that the SQUID data of Figs. 4(a) and (b) and that obtained by XMCD in Figs. 4(c) and (d) are both showing the ferromagnetism of the

1  
2  
3  
4  
5  
6 Mn layer despite the different probing depth of the two measurements, since it can be the  
7 only source of ferromagnetism in the present heterostructure system.  
8  
9

10 The heterostructure we have fabricated demonstrates various advantages compared to  
11 previously studied quantum anomalous Hall systems. First, it forms spontaneously by  
12 depositing Mn and Se on top of  $\text{Bi}_2\text{Se}_3$ . We have done this using thin films, but in principle it  
13 should also be possible to do this for single crystals or even thinner films. This is in contrast  
14 to the extensively studied systems with an intentional magnetic impurity doping,<sup>7-9,16,17</sup> in  
15 which fine-tuning of the impurity concentration is needed to achieve a long range magnetic  
16 order.<sup>32</sup>  
17  
18

19 Secondly, in our samples, we have an ideal situation where the Dirac cone and the  
20 magnetic layer interact strongly due to the spatial overlap of the respective wave functions,  
21 thus leading to a large magnetic gap but with minimal effects on other bands. This is in  
22 contrast to heterostructures that utilize the magnetic proximity effect.<sup>22-24</sup>  
23  
24

25 Thirdly, our samples are free from inhomogeneity since the structure was clearly determined  
26 by LEED measurements. This allowed us to observe a clear Dirac cone gap with ARPES and  
27 assign its origin unambiguously as due to the time-reversal symmetry breaking. Recalling  
28 that the presence of the impurity states makes it difficult to determine the gap opening in  
29 the Dirac cone as well as its origin,<sup>16,17</sup> this is a merit. Furthermore, the clear gap opening  
30 in ARPES means that our heterostructure does not show strong fluctuations of the magnetic  
31 energy gap.<sup>11</sup>  
32  
33

34 Finally, the Curie temperature of the heterostructure is above room temperature. Furthermore,  
35 the Dirac-cone gap is larger than the thermal fluctuation at room temperature. Therefore,  
36 we can expect to observe the QAHE for our samples at higher temperatures than those  
37 previously reported<sup>8-10</sup> by moving the Fermi level into the induced gap either chemically<sup>7</sup> or  
38 by gating.<sup>8,10,32</sup> So our heterostructure may be used in application for developing “topotronics”  
39 devices.  
40  
41  
42  
43  
44  
45  
46  
47  
48  
49  
50  
51  
52  
53  
54  
55  
56  
57  
58  
59  
60

### *Experimental and calculation methods*

The heterostructure samples were prepared by molecular beam epitaxy in ultrahigh vacuum (UHV) chambers equipped with a reflection-high-energy electron diffraction (RHEED) system. First, a clean Si(111)- $7 \times 7$  surface was prepared on an *n*-type substrate by a cycle of resistive heat treatments. The Si(111) $\beta\sqrt{3} \times \sqrt{3}$ -Bi surface was formed by 1 ML ( $7.83 \times 10^{14} \text{ cm}^{-2}$ ) of Bi deposition on the  $7 \times 7$  surface at 620 K monitored by RHEED. Then Bi was deposited on the  $\beta\sqrt{3} \times \sqrt{3}$ -Bi structure at  $\sim 200$  °C in a Se-rich condition. Such a procedure is reported to result in a smooth epitaxial film formation with the stoichiometric ratio of Bi:Se=2:3.<sup>33,34</sup> The grown Bi<sub>2</sub>Se<sub>3</sub> films were annealed at  $\sim 240$  °C for 5 minutes. The thickness of the Bi<sub>2</sub>Se<sub>3</sub> films in this work is  $\sim 15$  QL, which does not show the gap opening in the Dirac cone due to finite-size effects,<sup>34,35</sup> as shown in Fig. 1(a). Finally, Mn was deposited on Bi<sub>2</sub>Se<sub>3</sub> in a Se-rich condition at  $\sim 240$  °C. As reported in Ref.,<sup>25</sup> this results in a flat film formation which was believed to be a heterostructure of MnSe/Bi<sub>2</sub>Se<sub>3</sub>.

ARPES and SARPES measurements were performed *in situ* after the sample preparation. The ARPES measurements were performed at BL-5U and 7U of UVSOR-III using *p*-polarized photons in the energy range of 30-65 eV and 7.5-28 eV, respectively.<sup>36</sup> All the data shown were taken at 30 K unless otherwise indicated. The energy and angular resolutions were 15 meV and 0.25°, respectively. The SARPES measurements were performed at BL-9B of HiSOR using *p*-polarized photons in the energy of 18-21 eV at 30 K.<sup>37</sup> In some of the measurements, a magnetic field as large as  $\sim 0.1$  T was applied to the sample. The energy and angular resolutions were 30 meV and 0.75°, respectively.

LEED measurements were also performed *in situ* after the sample formation in another UHV chamber. The LEED patterns with incident energy from 80 to 400 eV were recorded in steps of 1 eV by a digital CCD camera at 100 K. *IV* curves of 14 inequivalent diffraction spots were obtained. In order to determine the surface structure, we calculated the *IV* curves in the tensor LEED to fit the experimental *IV* curves using the SATLEED package of Barbieri/Van Hove<sup>38</sup> and minimized Pendry's R-factor ( $R_p$ ). As shown in Fig. 2(b), each

1  
2  
3  
4  
5  
6  
7 atomic layer was treated differently according to their environments. The in-plane lattice  
8 constant of the heterostructure was determined from positions of the LEED spots as well  
9 as the RHEED spots and was the same with that of  $\text{Bi}_2\text{Se}_3$ . Angular momentum up to 17  
10 ( $l_{max} = 17$ ) was taken into account because of the strong scattering of the heavy Bi atom  
11 ( $Z = 83$ ). Considering the mean penetration depth of the incident electrons of  $\sim 10$  Å, only  
12 the topmost 7 surface layers were allowed to relax and we used the bulk  $\text{Bi}_2\text{Se}_3$  parameters  
13 for the layers beneath. In search of the optimal structure, the Debye temperature of each  
14 atom was changed in steps of 10 K from 50 K up to 300 K. If MnSe grew on  $\text{Bi}_2\text{Se}_3$ , it should  
15 have the  $p3m1$  symmetry. However, the symmetrically inequivalent spots, such as (1,0) and  
16 (0,1) spots, exhibited almost the same  $IV$  curves. Since this was also seen for the pristine  
17  $\text{Bi}_2\text{Se}_3$  LEED patterns, it probably comes from the fact that there are twin domains on the  
18 surface which are related by a  $180^\circ$  rotation. The superposition of the two domains should  
19 lead to the apparent twofold symmetry. Taking this double-domain surface into account, we  
20 took the average of the  $IV$  curves both in the calculation and in the experimental data such  
21 that  $\{h,k\}$  is the average of  $(h,k)$  and  $(k,h)$  spots (see Fig. 2(a)). Note that spots having the  
22 same mirror indices of  $h$  and  $k$  do not need averaging.  
23  
24  
25  
26  
27  
28  
29  
30  
31  
32  
33  
34  
35  
36  
37

38 For the SQUID measurements, the fabricated samples were capped with  $\sim 15$  nm of Se  
39 before taking it out of the UHV chamber and a commercial MPMS-52 system (Quantum  
40 Design) was used. The diamagnetic contribution of the Si substrate was derived from the  
41 field-dependent magnetization curves at room temperature and subtracted from all data.  
42  
43  
44  
45

46 XMCD measurements were performed at BL-4B of UVSOR-III with circularly polarized  
47 X-ray radiation (positive helicity with the polarization of 0.6) at 7.2 K and a magnetic field  
48 as high as  $\pm 5$  T was applied to the sample.<sup>39</sup> Instead of changing the photon polarization,  
49 we reversed the direction of the magnetic field to derive the XMCD spectra. As shown  
50 in Fig. 4(c),  $+(-)$  magnetic field corresponds to the direction antiparallel (parallel) to the  
51 direction of the photon incidence. The measurements were first performed for the samples  
52 with Se-capping. After measuring, the Se-capped samples were annealed at  $\sim 240$  °C to  
53  
54  
55  
56  
57  
58  
59  
60

1  
2  
3  
4  
5  
6  
7  
8  
9  
10  
11  
12  
13  
14  
15  
16  
17  
18  
19  
20  
21  
22  
23  
24  
25  
26  
27  
28  
29  
30  
31  
32  
33  
34  
35  
36  
37  
38  
39  
40  
41  
42  
43  
44  
45  
46  
47  
48  
49  
50  
51  
52  
53  
54  
55  
56  
57  
58  
59  
60

remove the capping layers. LEED observations showed a clear recovery of the  $1 \times 1$  surface periodicity for the cap-removed samples.

For structural optimization and electronic band calculations we used the Vienna Ab Initio Simulation Package<sup>40,41</sup> with generalized gradient approximation (GGA-PBE)<sup>42</sup> to the exchange-correlation potential. The interaction between the ion cores and valence electrons was described by the projector augmented-wave method.<sup>43,44</sup> The Hamiltonian contains scalar relativistic corrections, and the spin-orbit interaction (SOI) is taken into account by the second variation method.<sup>45</sup> To correctly describe the highly correlated Mn-*d* electrons we include the correlation effects within the GGA+*U* method.<sup>46</sup> The in-plane lattice constant of the heterostructure was fixed to that of Bi<sub>2</sub>Se<sub>3</sub>. DFT-D3 van der Walls corrections<sup>47</sup> were applied for accurate structure optimization. The Chern number was calculated for a symmetric MnBi<sub>2</sub>Se<sub>4</sub>/5QL-Bi<sub>2</sub>Se<sub>3</sub>/MnBi<sub>2</sub>Se<sub>4</sub> slab by using the method based on tracking the evolution of hybrid Wannier functions realized in Z2Pack.<sup>48</sup>

## Acknowledgement

The authors thank A. V. Matetskiy, A. A. Saranin, O. Rader, and A. Kimura for discussions. This work has been supported by Grants-In-Aid from Japan Society for the Promotion of Science (Nos. 15H05453, 16K13683, 19340078, 23244066), the Toray Science Foundation, the Basque Country Government, Departamento de Educación, Universidades e Investigación (Grant No. IT-756-13), the Spanish Ministry of Science and Innovation (Grant Nos. FIS2010-19609-C02-01, FIS2013-48286-C02-02-P, and FIS2013-48286-C02-01-P), the Tomsk State University Academic D.I. Mendeleev Fund Program (Grant No. 8.1.05.2015), and Saint Petersburg State University (project 15.61.202.2015). The ARPES experiments were performed under the UVSOR Proposal Nos. 25-808, 26-531, 27-533, 28-526, and S-15-MS-0034 and the SARPES experiments were performed under the HiSOR Proposal No. 15-A-14. The XMCD measurements were performed under the UVSOR proposal number S-16-MS-2017. The LEED measurements

1  
2  
3  
4  
5  
6 were performed under the ISSP Proposal number H17-A250. The SQUID measurements  
7  
8 were performed using facilities of the Cryogenic Research Center, the University of Tokyo.  
9  
10 Calculations were performed on the SKIF-Cyberia supercomputer at the National Research  
11  
12 Tomsk State University.  
13  
14

## 15 16 Supporting Information Available

17  
18  
19 The following files are available free of charge. Additional details on ARPES, SARPES,  
20  
21 *ab initio* calculations, SQUID, and XMCD measurements. This material is available free of  
22  
23 charge via the Internet at <http://pubs.acs.org>.  
24  
25  
26

## 27 28 References

- 29  
30  
31 (1) [https://www.nobelprize.org/nobel\\_prizes/physics/laureates/2016/](https://www.nobelprize.org/nobel_prizes/physics/laureates/2016/)  
32  
33  
34 (2) Hasan, M. Z.; Kane, C. L., Colloquium: Topological insulators. *Rev. Mod. Phys.* **2010**  
35  
36 82, 3045.  
37  
38 (3) Qi, X.-L.; Zhang, S.-C. Topological insulators and superconductors. *Rev. Mod. Phys.*  
39  
40 **2011** 83, 1057.  
41  
42  
43 (4) Qi, X.-L.; Li, R.; Zang, J.; Zhang, S.-C., Inducing a Magnetic Monopole with  
44  
45 Topological Surface States. *Science* **2009** 323 1184.  
46  
47  
48 (5) Haldane; F. D. M., Model for a quantum Hall effect without Landau levels:  
49  
50 Condensed-matter realization of the parity anomaly. *Phys. Rev. Lett.* **1988** 61, 2015.  
51  
52  
53 (6) Qi, X.-L.; Hughes, T. L.; Zhang, S.-C; Topological field theory of time-reversal invariant  
54  
55 insulators. *Phys. Rev. B* **2008** 78, 195424.  
56  
57  
58 (7) Xu, S.-Y. et al. Hedgehog spin texture and Berry's phase tuning in a magnetic  
59  
60 topological insulator. *Nature Phys.* **2012** 8, 616.



- 1  
2  
3  
4  
5  
6 (8) Chang, C.-Z. et al. Experimental Observation of the Quantum Anomalous Hall Effect  
7 in a Magnetic Topological Insulator. *Science* **2013** *340*, 167.  
8  
9  
10  
11 (9) Bestwick, A. J. et al. Precise Quantization of the Anomalous Hall Effect near Zero  
12 Magnetic Field. *Phys. Rev. Lett.* **2015** *114*, 187201.  
13  
14  
15  
16 (10) Chang C.-Z. et al. High-precision realization of robust quantum anomalous Hall state  
17 in a hard ferromagnetic topological insulator. *Nat. Mat.* **2015** *14*, 473.  
18  
19  
20  
21 (11) Lee, I. et al. Imaging Dirac-mass disorder from magnetic dopant atoms in the  
22 ferromagnetic topological insulator  $\text{Cr}_x(\text{Bi}_{0.1}\text{Sb}_{0.9})_{2-x}\text{Te}_3$ . *Proceeding of the National*  
23 *Academy of Sciences* **2015** *112*, 1316.  
24  
25  
26  
27 (12) Feng, X. et al. Thickness Dependence of the Quantum Anomalous Hall Effect in  
28 Magnetic Topological Insulator Films. *Adv. Mater.* **2016** *28*, 6386.  
29  
30  
31  
32 (13) Mogi, M. et al. Magnetic modulation doping in topological insulators toward  
33 higher-temperature quantum anomalous Hall effect. *Appl. Phys. Lett.* **2015** *107*,  
34 182401.  
35  
36  
37  
38 (14) Qi, S. et al. High-Temperature Quantum Anomalous Hall Effect in *n-p* Codoped  
39 Topological Insulators. *Phys. Rev. Lett.* **2016** *117*, 056804.  
40  
41  
42  
43 (15) Chang C.-Z. et al. Thin Films of Magnetically Doped Topological Insulator with  
44 Carrier-Independent Long-Range Ferromagnetic Order. *Adv. Mater.* **2013** *25*, 1065.  
45  
46  
47  
48 (16) Sessi, P. et al. Dual nature of magnetic dopants and competing trends in topological  
49 insulators. *Nature Commun.* **2016** *7*, 12027.  
50  
51  
52  
53 (17) Sánchez-Barriga J. et al. Nonmagnetic band gap at the Dirac point of the magnetic  
54 topological insulator  $(\text{Bi}_{1-x}\text{Mn}_x)_2\text{Se}_3$ . *Nature Commun.* **2016** *7*, 10559.  
55  
56  
57  
58 (18) Shiomi, Y. et al. Spin-Electricity Conversion Induced by Spin Injection into Topological  
59 Insulators. *Phys. Rev. Lett.* **2014** *113*, 196601.  
60

- 1  
2  
3  
4  
5  
6  
7 (19) Rojas-Sánchez, J.-C. et al. Spin to Charge Conversion at Room Temperature by Spin  
8 Pumping into a New Type of Topological Insulator:  $\alpha$ -Sn Films. *Phys. Rev. Lett.* **2016**,  
9 *116*, 096602.  
10  
11  
12  
13 (20) Wang, H. et al. Surface-State-Dominated Spin-Charge Current Conversion in  
14 Topological-Insulator-Ferromagnetic-Insulator Heterostructures. *Phys. Rev. Lett.* **2016**  
15 *117*, 076601.  
16  
17  
18  
19 (21) Wei, P.; Katmis, F.; Assaf, B. A.; Steinberg, H.; Jarillo-Herrero, P.; Heiman, D.; and  
20 Moodera, J. S.; *Phys. Rev. Lett.* **2013** *110*, 186807.  
21  
22  
23  
24 (22) Ereemeev, S. V.; Men'shov, V. N.; Tugushev, V. V.; Chulkov, E. V., Interface induced  
25 states at the boundary between a 3D topological insulator  $\text{Bi}_2\text{Se}_3$  and a ferromagnetic  
26 insulator EuS. *J. Magn. Magn. Mater.* **2015** *383*, 30.  
27  
28  
29  
30  
31 (23) Katmis, F. et al. A high-temperature ferromagnetic topological insulating phase by  
32 proximity coupling. *Nature* **2016** *533*, 513.  
33  
34  
35  
36 (24) Ereemeev, S. V., Men'shov, V. N., Tugushev, V. V., Echenique, P. M. & Chulkov, E.  
37 V. Magnetic proximity effect at the three-dimensional topological insulator/magnetic  
38 insulator interface. *Phys. Rev. B* **2013** *88*, 144430.  
39  
40  
41  
42  
43 (25) Matetskiy, A. V. et al. Direct observation of a gap opening in topological interface  
44 states of  $\text{MnSe}/\text{Bi}_2\text{Se}_3$  heterostructure. *Appl. Phys. Lett.* **2015** *107*, 091604.  
45  
46  
47  
48 (26) Hsieh, D. et al. A tunable topological insulator in the spin helical Dirac transport  
49 regime. *Nature* **2009** *460*, 1101.  
50  
51  
52  
53 (27) Bianchi, M. et al. Coexistence of the topological state and a two-dimensional electron  
54 gas on the surface of  $\text{Bi}_2\text{Se}_3$ . *Nature Commun.* **2010** *1*, 128.  
55  
56  
57 (28) Nowka, C. et al. Chemical vapor transport and characterization of  $\text{MnBi}_2\text{Se}_4$ . *J. Cryst.*  
58 *Growth* **2017** *459*, 81.  
59  
60

- 1  
2  
3  
4  
5  
6 (29) Menshchikova, T. V., Otrokov, M. M., Tsirkin, S. S., Samorokov, D. A., Bebneva, V.  
7 V., Ernst, A., Kuznetsov, V. M., Chulkov, E. V., *Nano Lett.* **2013** *13* 6064.  
8  
9  
10  
11 (30) Thouless, D. J.; Kohmoto, M.; Nightingale, M. P.; den Nijs, M., Quantized Hall  
12 Conductance in a Two-Dimensional Periodic Potential, *Phys. Rev. Lett.* **1982** *49*, 405.  
13  
14  
15  
16 (31) The magnetization curve does not seem to saturating even at 5 T and shows a  
17 characteristic somewhat similar to a paramagnetic one. One possible explanation for  
18 this is the presence of Mn atoms at substitutional sites that give a paramagnetic  
19 contribution.  
20  
21  
22  
23  
24 (32) Chang, C.-Z. et al. Chemical-Potential-Dependent Gap Opening at the Dirac Surface  
25 States of Bi<sub>2</sub>Se<sub>3</sub> Induced by Aggregated Substitutional Cr Atoms. *Phys. Rev. Lett.* **2014**  
26 *112*, 056801.  
27  
28  
29  
30  
31 (33) Zhang, G. et al. Quintuple-layer epitaxy of thin films of topological insulator Bi<sub>2</sub>Se<sub>3</sub>.  
32 *Appl. Phys. Lett.* **2009** *95*, 053114.  
33  
34  
35  
36 (34) Sakamoto, Y., Hirahara, T., Miyazaki, H., Kimura, S.-I. & Hasegawa, S. Spectroscopic  
37 evidence of a topological quantum phase transition in ultrathin Bi<sub>2</sub>Se<sub>3</sub> films. *Phys. Rev.*  
38 *B* **2010** *81*, 165432.  
39  
40  
41  
42  
43 (35) Zhang, Y. et al. Crossover of the three-dimensional topological insulator Bi<sub>2</sub>Se<sub>3</sub> to the  
44 two-dimensional limit. *Nature Phys.* **2010** *6*, 584.  
45  
46  
47  
48 (36) Kimura, S.-I. et al. SAMRAI: A novel variably polarized angle-resolved photoemission  
49 beamline in the VUV region at UVSOR-II. *Rev. Sci. Instrum.* **2010** *81*, 053104.  
50  
51  
52  
53 (37) Okuda, T. et al. Efficient spin resolved spectroscopy observation machine at Hiroshima  
54 Synchrotron Radiation Center. *Rev. Sci. Instrum.* **2011** *82*, 103302.  
55  
56  
57 (38) Van Hove, M. A. et al. Automated determination of complex surface structures by  
58 LEED. *Surf. Sci. Rep.* **1993** *19*, 191.  
59  
60

- 1  
2  
3  
4  
5  
6  
7 (39) Nakagawa, T.; Takagi, Y.; Matsumoto, Y; Yokoyama, T., Enhancements of Spin and  
8 Orbital Magnetic Moments of Submonolayer Co on Cu(001) Studied by X-ray Magnetic  
9 Circular Dichroism Using Superconducting Magnet and Liquid He Cryostat. *Jpn. J.*  
10 *Appl. Phys.* **2008** *47*, 2132.  
11  
12  
13  
14  
15 (40) Kresse, G.; Hafner, J., *Ab initio* molecular dynamics for open-shell transition metals.  
16 *Phys. Rev. B* **1993** *48*, 13115.  
17  
18  
19  
20 (41) Kresse, G. & Furthmüller, J. Efficient iterative schemes for *ab initio* total-energy  
21 calculations using a plane-wave basis set. *Phys. Rev. B* **1996** *54*, 11169.  
22  
23  
24  
25 (42) Perdew, J. P.; Burke, K.; Ernzerhof, M., Generalized gradient approximation made  
26 simple. *Phys. Rev. Lett.* **1996** *77*, 3865.  
27  
28  
29  
30 (43) Blöchl, P. E., Projector augmented-wave method. *Phys. Rev. B* **1994** *50*, 17953.  
31  
32  
33 (44) Kresse, G.; Joubert, D., From ultrasoft pseudopotentials to the projector  
34 augmented-wave method. *Phys. Rev. B* **1999** *59*, 1758.  
35  
36  
37 (45) Koelling, D. D.; Harmon, B. N., A technique for relativistic spin-polarised calculations.  
38 *J. Phys. C* **1977** *10*, 3107.  
39  
40  
41  
42 (46) Liechtenstein, A. I.; Anisimov, V. I.; Zaanen, J., Density-functional theory and strong  
43 interactions: Orbital ordering in Mott-Hubbard insulators. *Phys. Rev. B* **1995** *52*,  
44 R5467.  
45  
46  
47  
48  
49 (47) Grimme, S.; Antony, J.; Ehrlich, S.; Krieg, H., A consistent and accurate *ab initio*  
50 parametrization of density functional dispersion correction (DFT-D) for the 94 elements  
51 H-Pu. *J. Chem. Phys.* **2010** *132*, 154104.  
52  
53  
54  
55 (48) Soluyanov, A. A.; Vanderbilt, D., Computing topological invariants without inversion  
56 symmetry. *Phys. Rev. B* **2011** *83*, 235401.  
57  
58  
59  
60

## Graphical TOC Entry

